Revision 1

Word Count: 6285

Mixing of cogenetic magmas in the Cretaceous Zhangzhou calc-alkaline granite from SE China recorded by in-situ apatite geochemistry

Xiaobing Zhang[1, 2], Feng Guo[1]*, Bo Zhang[1, 2], Liang Zhao[1], Guoqing Wang[1, 2]

1 State Key Laboratory of Isotope Geochemistry, Guangzhou Institute of Geochemistry, Chinese Academy of Sciences, Guangzhou 510640, China

2 College of Earth and Planetary Sciences, University of Chinese Academy of Sciences, Beijing 100049, China

Corresponding author: Feng Guo *(guofengt@263.net)*

Abstract

Mixing of cogenetic magmas represents an important process in granite petrogenesis but is difficult to identify, and is consequently often overlooked, due to the absence of obvious isotopic distinctions between the mixed melts. We have conducted *in-situ* elemental and O isotope analyses on apatite from Cretaceous Zhangzhou calc-alkaline granite in SE China. We integrated these data with microanalyses on other minerals (plagioclase, zircon and titanite) as well as whole-rock geochemistry to decipher the mixing history of this granitic complex. The apatite occurs as an early crystallizing phase forming inclusions in biotite, plagioclase and titanite, and is characterized by core-rim zonation textures with a dark core and bright rims in back-scattered images. The core domains have remarkably higher SO_3 and Li concentrations but much lower SiO_2, REE, and Y concentrations than the rim domains. However, both the cores and rims show geochemical compositions similar to that from typical I-type granite and also have mantle-like O isotope compositions (the core has $\delta^{18}O$ = 5.3-6.8‰ and the rim has $\delta^{18}O$ = 5.2-6.4‰, respectively), indicating crystallization from granitic melts derived from newly accreted crust. The combined major and trace element and O isotope compositions of apatite and whole-rock geochemistry suggests that compositional evolution of the Zhangzhou granite involved mixing between two cogenetic magma batches, with variable degrees of subsequent differentiation. Batch I magma was a low-SiO_2 and high-SO_3 melt, whereas Batch II magma was a high-SiO_2 and low-SO_3 melt that experienced

devolatilization. The high S content in apatite cores further suggests the parental magma of the Zhangzhou granite likely originated from a sulfur-rich source comprising mainly newly accreted arc crust in response to subduction of the paleo-Pacific Ocean. The geochemical records of these magmatic processes are rarely observed in coeval zircon, titanite and plagioclase. Our study therefore demonstrates that apatite geochemistry is potentially a more suitable monitor of complex magmatic evolution, including devolatilization and mixing of isotopically indistinguishable magmas.

Keywords: Apatite geochemistry; mixing; devolatilization; cogenetic magmas; Cretaceous; SE China

Introduction

Granitic rock (hereafter simply referred to as granite) is a major constituent of the upper continental crust and contains abundant mineral resources essential for sustained economic development. The compositions of granite vary extensively and can be broadly divided into I-, S-, M- and A-type based on geochemical features and melting sources (Chappell and White 1974; Whalen et al. 1987). Many petrogenetic hypotheses, e.g., fractional crystallization, assimilation via fractional crystallization (AFC, DePaolo 1981), and magma mixing (Griffin et al. 2002), have been proposed to interpret the geochemical diversity of granite. Nevertheless, it remains difficult to fully understand the magmatic evolution of granite since clear geochemical evidence

for many hypothesized petrogenetic processes is lacking.

Recent techniques in studying chemistry and isotopic composition of minerals such as plagioclase, titanite, zircon and apatite have become widely used petrogenetic tools in supplementing or even replacing conventional bulk-rock analyses (e.g., Streck 2008; Lisowiec et al. 2015; Nathwani et al. 2020). However, the sensitivity or applicability of these minerals in tracking magmatic processes is extremely variable because they each partition (or exclude) elements (or isotopes) of specific geochemical behavior and are typically relevant to only parts of a given crystallization sequence. Minerals that indelibly record geochemical proxies of changing magma compositions over a wide crystallization interval are rare.

Apatite is one such mineral, containing measurable concentrations of a range of elements of various geochemical behavior, including halogens, S, rare earth elements (REEs), Sr, Y (Ayers and Watson 1993; Pan and Fleet 2002; Marks et al. 2012; Harlov 2015; Webster and Piccoli 2015; Bruand et al. 2017), that are sensitive to specific magmatic/petrogenetic processes. For example, the textural and compositional variations in apatite from the Pingtan complex in SE China records both magmatic evolution and post-crystallization fluid activity regardless of a narrow range in Nd isotopic composition (Zhang et al. 2020). As a near-liquidus phase, apatite crystallizes early in metaluminous felsic magma (Piccoli and Candela 2002; Webster and Piccoli 2015) and hence records early high-temperature magma compositional variations. Subsequent changes in magma composition can be reflected in compositional zonations of apatite because of the insignificant intracrystalline elemental diffusion

rates, especially for REE, S and Si (e.g., Dowty 1980; Tepper and Kuehner 1999; Cherniak 2010). Accordingly, apatite may have significant advantages in terms of deciphering magmatic evolution trends and processes compared with other commonly used minerals such as plagioclase, titanite and zircon.

In this contribution, we present detailed petrographic observations and systematic *in-situ* geochemical analyses (major and trace element compositions and O and Sr isotopes) on apatite, zircon, titanite and plagioclase from granite of Zhangzhou igneous complex, SE China. These new data, together with whole-rock geochemistry, provide a fresh perspective on the role of mixing between cogenetic magmas involved in the generation of Zhangzhou calc-alkaline granite and show the advantage of using apatite geochemistry to track the magmatic evolution of granitoid batholiths.

Geological backgrounds

The geology of South China consists of Yangtze block in the northwest and Cathaysia block in the southeast, which were amalgamated in the Neoproterozoic along the Jiangnan Orogenic Belt (Fig. 1; Zhang et al. 2013). It underwent extensive tectonic and magmatic activity associated with the subduction of paleo-Pacific Ocean during Mesozoic (Zhou et al. 2006). The distribution of Mesozoic igneous rocks in SE China is mainly controlled by several large-scale NE-trending faults such as the Zhenghe-Dafu and Changle-Nan'ao faults. The magmatism consists of predominant

felsic lavas with minor intrusive mafic rocks (Zhou et al. 2006; Xu et al. 2020). Granitic rocks exposed in this region are mainly shallow-level, calc-alkaline, I-type granitoids that range from granodiorite, monzogranite to alkali-feldspar granite (Zhou et al. 2006; Li et al. 2014). These rocks also show hybrid geochemical signatures reflecting crust-mantle interaction that are typically observed at subduction zones (e.g., Griffin et al. 2002; Zhou et al. 2006; Guo et al. 2012; Xu et al. 2020). The contemporaneous mafic intrusive rocks are mainly hornblende gabbros, which show geochemical features similar to mafic arc cumulates (e.g., Li et al. 2014; Zhang et al. 2019).

The Zhangzhou batholith is located in the coastal region of Fujian province, SE China. Previous studies showed emplacement ages of this batholith ranging from 97 to 107 Ma (Chen et al. 2013). The calc-alkaline granite occurs as the main body of the batholith, consisting of granodiorite and monzogranite. In the field, abundant mafic microgranular enclaves (MMEs) occur in the monzogranite and both show a sharp contact relationship (Fig. 2a and b). The granodiorite is equigranular and consists of plagioclase (~45 vol.%), K-feldspar (~25 vol.%), quartz (~20 vol.%) and biotite (5-8 vol.%), with accessory zircon, apatite, titanite, allanite and epidote. The major minerals in the monzogranite are K-feldspar (~35 vol.%), quartz (~30 vol.%), plagioclase (~ 25 vol.%) and biotite (~5 vol.%), with accessory zircon, apatite, allanite and Fe-Ti oxides. The MMEs consist of plagioclase, biotite and quartz, with or without K-feldspar, and accessory minerals include apatite, zircon, titanite, allanite,

and Fe-Ti oxides (Chen et al. 2013). In the granite, apatite occurs as euhedral inclusions hosted in biotite, plagioclase and titanite (Fig. 2c-f). Based on field observations and geochemical studies, Chen et al. (2013) proposed that the calc-alkaline granite in the Zhangzhou batholith was formed by mixing between mantle- and crust-derived magmas.

Analytical methods

Whole-rock geochemical analyses

Whole-rock major oxides were determined by wavelength X-ray fluorescence spectrometry (XRF) at the Sample Solution Analytical Technology Co., Ltd., Wuhan, China. About 0.5g of powder was thoroughly mixed with 3.6g $Li_2B_4O_7$, 0.4g LiF, 0.3g NH_4NO_3, and minor LiBr in a platinum crucible. It was then melted in a furnace to form a glass disk for major element analysis. Trace element concentrations of the samples were determined by a Perkin-Elmer ELAN 6000 inductively coupled plasma mass spectrometry (ICP-MS) after acid digestion in high-pressure Teflon bombs at Guangzhou Institute of Geochemistry (GIG), Chinese Academy of Sciences (CAS). This involved mixing ~50 mg sample powder with 1 mL HF and 0.5 mL HNO_3 in a Teflon beaker. Then the Teflon beaker was sealed in a stainless-steel bomb and heated at 190°C for 48 hours. The detailed analytical procedure was reported by Liu et al. (1996). The analytical errors were 5% for rare earth element (REE) and high field strength element (HFSE), and 5 to ~ 10% for the other elements, based on repetitive

136 analyses of USGS standards GSR-1 (granite), GSR-2 (andesite) and GSR-3 (basalt).

137 Whole-rock Sr and Nd isotope analyses were performed with a Finnigan
138 Neptune multi-collector ICP-MS at the GIG-CAS, following the analytical procedures
139 described by Li et al. (2006). The REE and Sr were separated via cation columns, and
140 Nd fractions were further separated by HDEHP-coated Kef columns. The procedural
141 blanks were less than 200 pg for Sr and about 30 pg for Nd. The measured $^{87}Sr/^{86}Sr$
142 and $^{143}Nd/^{144}Nd$ ratios were normalized to $^{86}Sr/^{88}Sr = 0.1194$ and $^{146}Nd/^{144}Nd =$
143 0.7219, respectively. The reported $^{87}Sr/^{86}Sr$ and $^{143}Nd/^{144}Nd$ ratios were adjusted to
144 the NBS SRM 987 standard ($^{87}Sr/^{86}Sr=0.710247 \pm 8$, 2σ) and the JNdi-1 standard
145 ($^{143}Nd/^{144}Nd= 0.512115 \pm 4$, 2σ, n=4), respectively. Repeated analyses of NBS SRM
146 987 standard and the Shin Etsu JNdi-1 standard separately yielded mean values of
147 0.710247 ± 9 and 0.512115 ± 6 (2σ, n = 3). During whole-rock Sr-Nd isotope
148 analyses, the USGS reference BHVO-2 (basalt) yielded $^{87}Sr/^{86}Sr = 0.703475 \pm 8$ (2σ,
149 n = 6), $^{143}Nd/^{144}Nd = 0.512981 \pm 5$ (2σ, n = 6), consistent with the recommended
150 values reported in Weis et al. (2005).

151 **Electron microprobe (EMP) analysis**

152 Backscattered electron (BSE) and cathodoluminescence (CL) images were
153 performed with a SUPRA 55 SAPPHIRE equipped with a secondary electron and
154 energy-dispersive X-ray spectrometry (EDS) detector. The concentrations of major
155 elements in apatite, titanite, and plagioclase were determined by a Cameca SX FiveFe
156 electron microprobe and JOEL JXA-8100 electron microprobe at the GIG-CAS. The

operating conditions were 15 kV accelerating voltage, 20 nA probe current, and 5 μm spot diameter. The standards for adjustment include apatite for Ca and P, fluorite for F, sodalite for Cl, albite for Na, sanidine for K, Si and Al, pyroxene for Mn, Fe, and Mg, and rutile for Ti respectively. The analytical errors were within 1%.

LA-ICP-MS trace element analysis

Trace-element analyses of apatite, titanite and zircon were performed with a Resolution M-50 laser ablation (LA) system coupled to an Agilent 7900a type inductively coupled plasma-mass spectrometer (ICP-MS) at the GIG-CAS. The detailed analytical procedure was reported in Tu et al. (2011). The diameter of the laser beam was 31μm for zircon, apatite and titanite (with 80 mJ laser energy, 6 Hz ablation frequency). Helium gas carrying the ablated sample aerosol is mixed with argon carrier gas prior to introduction into the ICP-MS. Each analysis included approximately 20 s of background acquisition (from a gas blank) followed by 45 s of data acquisition. ^{43}Ca was used as the internal standard for apatite and titanite and ^{29}Si was used as the internal standard for zircon. The content of CaO in apatite and titanite was measured by EMPA and SiO_2 in zircon was assumed to be stoichiometric in zircon with a concentration of ca. 32.8 wt%. NIST SRM 610 and 612 were employed as external standards, respectively, which were analyzed twice after every 8 sample analyses. Data reduction was performed off-line by the ICPMSDataCall software (Liu et al. 2008). The corresponding mean element concentrations of standards during this study are listed after the trace element concentrations for apatite, zircon and titanite

178 respectively.

179 ***In-situ* Sr isotopic analysis of plagioclase**

180 All *in-situ* Sr isotope analyses in this study were performed on a Neptune Plus
181 MC-ICP-MS (Thermo Scientific), coupled with a RESOlution M-50 193 nm laser
182 ablation system (Resonetics) at the GIG-CAS. The laser parameters were set as follow:
183 beam diameter, 112-155 μm; repetition rate, 6 Hz; energy density, ~4 J cm^{-2}. Each
184 analysis consisted of 250 cycles with an integration time of 0.262 s per cycle. During
185 the first 30s, the gas blank of the system was monitored with the laser beam off. In the
186 following 30s, the signals of ablated plagioclase were collected with the laser beam on.
187 The gas blank of ^{83}Kr and ^{88}Sr were less than 2.5 mv and 0.5 mv during the
188 measurement of this study. The interferences of ^{84}Kr and ^{86}Kr on ^{84}Sr and ^{86}Sr were
189 corrected by subtracting gas blank from the raw time-resolved signal intensities. The
190 mass bias of $^{87}Sr/^{86}Sr$ was normalized to $^{86}Sr/^{88}Sr = 0.1194$ with an exponential law.
191 The detailed data reduction procedure is reported in Zhang et al. (2015). Repeated
192 analyses of the external standard NKT-1G yielded a weighted $^{87}Sr/^{86}Sr$ value of
193 0.70355 ± 0.00003 (2SD, n = 7), which is consistent with the reference value
194 (0.70351 ± 0.00002, Elburg et al. 2005). The corresponding standard data during this
195 study are listed after the Sr isotope of plagioclase.

196 ***In-situ* O isotope analyses of apatite and zircon**

197 *In-situ* oxygen isotope compositions of apatite were obtained using the Cameca

198 IMS-1280 SIMS at the Institute of Geology and Geophysics, CAS. Separated apatite
199 grains were embedded in epoxy disks together with apatite standards (Qinghu and
200 Durango apatite). The Cs^+ primary ion beam was accelerated at 10 kV, with an
201 intensity of ~2 nA, with spot sizes of about 20 μm in diameter. The normal-incidence
202 electron flood gun was used to compensate for the charge at the surface of the
203 gold-coated samples. Oxygen isotopes were measured using multi-collection mode on
204 two off-axis Faraday cups. The analytical procedures of apatite were similar to those
205 used for zircon oxygen isotopes as described by Li et al. (2010). *In-situ* oxygen
206 isotopes of zircon were also obtained using the Cameca IMS-1280 HR SIMS at the
207 GIG-CAS. The analytical procedures of zircon are described by Xia et al. (2019).
208 Measured $^{18}O/^{16}O$ ratios were normalized by using Vienna Standard Mean Ocean
209 Water and compositions ($V_{VSMOW,}$ $^{18}O/^{16}O$ = 0.0020052), reported in standard per mil
210 notation, and corrected for the instrumental mass fractionation factor (IMF). The IMF
211 was obtained using the Durango fluorapatite and Penglai zircon as references for
212 apatite and zircon, respectively. The average value of measured $\delta^{18}O$ of Durango
213 apatites was 10.15‰ (2SD = 0.56, n = 26), which is similar to the result in Trotter et
214 al. (2008). The Qinghu apatite was also analyzed as an external reference for apatite,
215 with a $\delta^{18}O$ value of 5.59‰ (2SD = 0.52, n = 31). The $\delta^{18}O$ values of the Durango and
216 Qinghu apatite and Penglai and Qinghu zircon are listed after the $\delta^{18}O$ values for
217 apatite and zircon, respectively.
218

Results

Whole-rock geochemistry

Whole-rock compositions are listed in Supplementary Table S1. The rocks of the Zhangzhou batholith show large variations in SiO_2 contents. The gabbro and diorite together have SiO_2 ranging from 49.9 to 60.1 wt% with relatively high Mg-number (Mg # = 48 to 52). The calc-alkaline granites (monzogranites and granodiorites) span a SiO_2 range from 63.0 to 71.0 wt%, with a Mg-number ranging from 34 to 43. The granites are metaluminous with A/CNK between 0.92 and 0.99. Monzogranites (Sample No. 17ZZ05 and 17ZZ06) generally contain higher SiO_2 content than the granodiorites (67.8 -71.0 wt% vs. 63.0-66.8 wt%), ∑REE (212-309 ppm vs. 135-235 ppm) and K_2O (3.59-4.51 wt% vs. 2.83-3.50 wt%) but lower CaO (2.22 to 2.87 wt% vs. 3.86-4.79 wt%) and MgO (0.79-1.12 vs. 1.33-2.07 wt%). In contrast, the alkali feldspar granite has the highest SiO_2 content with a range from 76.4 to 77.6 wt% and the lowest Mg-number (Mg# = 16 to 22). All rock types have similar initial $^{87}Sr/^{86}Sr$ ratios, ranging from 0.70602 to 0.70742. The mafic rocks have $\varepsilon_{Nd}(t)$ values ranging from -2.7 to -2.8, while the felsic rocks have slightly lower $\varepsilon_{Nd}(t)$ values between -3.2 and -4.2 (Supplementary Table S1). Thus, the mafic and felsic rocks together form an igneous complex with almost similar isotope compositions.

Texture and geochemistry of apatite

Representative BSE images for apatite from the calc-alkaline granite are

239 presented in Fig. 3. These apatite grains are mostly prismatic with sizes ranging from
240 100 to 200 μm (Figs. 2c-f and 3). They commonly occur as inclusions hosted in the
241 major mineral phases (Fig. 2c-f), indicating apatite was an early crystallizing phase.
242 Most of the apatite grains exhibit a core-rim zonation texture with a dark core and
243 bright rims in the BSE images (Fig. 3). The dark core spans a range of 30-100 μm in
244 size and the bright rims range from 20 to 40 μm in width (Fig. 3).

245 The compositions of the analyzed apatite are listed in Supplementary Table S2.
246 Both the apatite core and rim domains are fluorapatite with F > 2.5 wt% and F/Cl
247 ratio > 11.5 (Fig. 4a and b). They show similar P_2O_5 (41.1-43.3 wt%), CaO (53.4-57.9
248 wt%), FeO (0.01-0.12 wt%) and MnO (0.16-0.29 wt%). However, the apatite core
249 domains generally contain higher SO_3 (0.28-1.00 wt% vs. 0.10-0.42 wt%), Na_2O
250 (0.08-0.30 wt% vs. 0.02-0.11 wt%) and lower SiO_2 (0.01-0.20 wt% vs. 0.26-0.58 wt%)
251 contents than the rim domains. Also, the core domains generally have higher Li
252 concentrations (2.0 to 19.2 ppm vs. 0.6 to 4.3 ppm) but lower REE (∑REE = 3989 to
253 9743 ppm vs. 9380 to 16417 ppm) and Y (Y =259 to 894 ppm vs. 517 to 1781 ppm)
254 concentrations than the rim domains. Nevertheless, all apatite domains have relatively
255 high Ce/Y ratios, within the compositional fields of apatite from 'I-type granitoids'
256 (Fig. 4c, Laurent et al., 2017), and show right-declined chondrite-normalized REE
257 patterns with similar Ce/Ce* and Eu/Eu* ratios (Fig. 4d). Major and trace element
258 analyses from a profile across a representative zoned apatite grain show abrupt
259 compositional variations (Fig. 5, Supplementary Table S2). From core to rim, the SO_3
260 concentration decreases from 0.73 to 0.16 wt% and Cl decreases from 0.11 to 0.05

wt%, whereas SiO_2 increases from 0.27 to 0.70 wt% (Fig. 5b-d). The apatite rims have 6587 to 7009 ppm Ce and 866 to 1017 ppm Y, up to three times the concentrations in the core domain (Ce = 2354 to 2874 ppm, Y = 338 to 428 ppm, Fig. 5f and g). The apatite rims also have higher Sr (Sr = 223 to 230 ppm vs. 135 to 166 ppm, Fig. 5h). In contrast, the apatite cores contain 5.1-7.4 ppm Li and 0.11-0.18 wt% Na_2O, much higher than those in the rims (Li = 1.3-3.0 ppm, Na_2O= 0.03-0.04 wt%, Fig. 5e and i).

The O isotope compositions of apatite are listed in Supplementary Table S2 and plotted in Fig. 6. Both the apatite core and rim domains have mantle-like O isotopic compositions regardless of their difference in ∑REE (Fig. 6). The core domains have $\delta^{18}O$ values ranging from 5.3 ‰ (2SE = 0.28) to 6.8 ‰ (2SE = 0.26) with an average of 6.0 ‰ (n = 21), and the apatite rim domains have $\delta^{18}O$ values ranging from 5.2 ‰ (2SE = 0.32) to 6.4 ‰ (2SE = 0.37) with an average of 5.8 ‰ (n = 21).

Textures and geochemistry of other minerals

Zircon. The compositions of zircon are listed in Supplementary Table S3. Zircon is hosted in main mineral phases such as plagioclase and biotite. It exhibits a euhedral prismatic form, ranges from 50 to 200 μm in diameter with length/width ratios from 2:1 to 3:1, and typical igneous oscillatory zoning in CL images (Supplementary Materials, Fig. S1). The Hf concentration of zircon ranges from 7695 to 11489 ppm, is negatively correlated with the concentrations of Ti (3.1 to 16.7 ppm) and P (332 to 696 ppm) and with Th/U (0.54 to 1.48) and Eu/Eu* (0.4 to 1.2), but is positively

282 correlated with Yb/Gd (7.9 to 27.8). The Ti-in-zircon (T_{Ti-Zr}) thermometer yields
283 values ranging from 674 to 835°C (Supplementary Table S3) using the equations of
284 Ferry and Watson (2007). Zircon also has mantle-like $\delta^{18}O$ values ranging from 5.3 ‰
285 to 6.9 ‰ with an average of 5.8 ‰ (SD = 0.44, n = 20).

286 **Titanite.** The compositions of titanite are listed in Supplementary Table S4.
287 Titanite crystals always display continuous and oscillatory zoning in BSE images,
288 showing small intracrystalline compositional changes. Some titanite crystals show an
289 obvious zoned texture with a bright core and dark rim. The bright core often shows
290 fir-tree and oscillatory zonation. The dark rim shows a uniform texture and is
291 occasionally surrounded by bright domains (Supplementary Materials, Fig. S2).
292 Titanite frequently contains inclusions of the zoned apatite (Fig. 2e). Titanite from the
293 granites has weakly variable SiO_2 (29.02–30.74 wt%), TiO_2 (34.04–36.81wt%), CaO
294 (26.37–29.33 wt%), Al_2O_3 (1.02–1.65 wt%) and FeO (1.48–2.49 wt%) and F
295 (0.05-0.42 wt%). However, the total REE concentrations of titanite varies greatly
296 from 1.7 wt% to 2.9 wt%. The bright domains generally have much higher REE
297 concentrations than the dark parts.

298 **Plagioclase.** The compositions of plagioclase are listed in Supplementary Table
299 S5. Plagioclase crystals in the granite show complex textures and zoning patterns.
300 Some grains have a strong dissolution texture, with sodic patches in the dissolved
301 calcic cores and less calcic rims (Supplementary Fig. S3). The dissolved core has a
302 sieved texture and higher Ca contents (An_{38} - An_{48}), whereas the dark patches in the
303 core and the rim have lower Ca contents (An_{14} - An_{30}). Such a compositional zonation

might be caused during decompression of the magma. Twelve analytical spots on plagioclase from the granite show a narrow variation of initial $^{87}Sr/^{86}Sr$ ratios from 0.7064 to 0.7067 with an average of 0.7066 (n = 12). This value is quite similar to the host bulk rock ($^{87}Sr/^{86}Sr_{(i)}$ = 0.7066).

Discussion

Core-rim zonation texture in apatite: a record of magma mixing

The apatite in Zhangzhou granite is characterized by textural and compositional zonation with abrupt core to rim increases in SiO_2 and REE concentrations and decreases in SO_3 and Li (Figs. 3 and 5). Compositional zoning of minerals in igneous rocks results from various processes including fractional crystallization, AFC processes, post-crystallization hydrothermal activity and magma mixing. In the following, we discuss the possible effects of these processes on the compositional variations observed in the apatite from Zhangzhou granite.

(1) Fractional crystallization plays an important role in progressive mass and ionic exchange between magma and minerals. Compositional zonation in the crystallizing phase typically follows “normal” igneous trends (i.e., increases in incompatible elements and decreases in compatible elements from core to rims, Gao et al. 2007; Guo et al. 2007; Streck 2008). Since REEs behave as incompatible elements in plagioclase, biotite and quartz (Nash and Crecraft 1985) – the major

mineral assemblage in the Zhangzhou granite, fractionation of these minerals would lead to increasing REE concentrations in the crystallizing apatite. Biotite-dominated fractionation may also cause halogen variation in a crystallizing magma and possibly results in Cl/F zonation in apatite (Teiber et al. 2014; Ansberque et al. 2019). Fractionation of biotite + plagioclase + quartz might explain the core to rim increases in REE concentrations and decreasing Cl/F in zoned apatite from the Zhangzhou granite, but it cannot explain the observed rim to core trends to higher SiO_2 and Sr concentrations (Fig. 5b and h) and similar Fe concentrations. Fractional crystallization of significant amounts of apatite might explain progressive core to rim decreases in REE concentrations in zoned apatite (e.g., Bruand et al. 2014) because REEs are compatible in apatite (e.g., Prowatke and Klemme 2006). However, such trends contrast with the abrupt increase in concentration from the core to rim that we observe (Fig. 5f and g). In any case, fractional crystallization is a continuous process which likely forms continuous compositional zonations, or predictable changes reflected in changing modal mineral assemblages, e.g., a progressive increase of La in clinopyroxene from core to rim during fractional crystallization (Gao et al. 2007). Therefore, it is clear that the sharp core to rim compositional variations in apatite of the Zhangzhou granite could not be generated by fractional crystallization alone (Figs. 5 and 7).

(2) Similar to fractional crystallization, AFC processes also generally result in the crystallization of minerals with normal compositional zonation (e.g., Jung et al. 1999). However, in the Zhangzhou granite, there are weak correlations between the

346 $^{87}Sr/^{86}Sr_{(i)}$ and $\varepsilon_{Nd}(t)$ and SiO_2 (SiO_2 = 67.8-71.0 wt%, $^{87}Sr/^{86}Sr_{(i)}$ = 0.7062-0.7066,
347 and $\varepsilon_{Nd}(t)$= -3.0 to -4.2, Supplementary Table S1). The plagioclase in these granites,
348 with variable An contents, has a uniform Sr isotope composition (An=16-48,
349 $^{87}Sr/^{86}Sr_{(i)}$ = 0.7064-0.7067, Supplementary Table S5), similar to the whole rock value
350 ($^{87}Sr/^{86}Sr_{(i)}$ = 0.7066). Apatite core and rim domains as well as zircon have similar
351 oxygen isotope compositions (Supplementary Table 3). All these geochemical features
352 do not support a significant role for crustal contamination or assimilation.

353 (3) Hydrothermal fluids have been shown to leach REE from apatite, resulting in
354 substantial decreases in REE concentrations and variations in LREE/HREE ratios as
355 well as O isotopes in apatite with the formation of new REE-phosphates such as
356 monazite and xenotime (e.g., Rae et al. 1996; Harlov and Förster 2003; Harlov et al.
357 2005; Broom-Fendley et al. 2016; Zeng et al. 2016; Birski et al. 2019). Whilst apatite
358 crystals in the Zhangzhou granite have REE-poor cores, it is unlikely that this
359 compositional zonation resulted from post-crystallization hydrothermal activity
360 because the apatite core domains have La/Sm ratio and $\delta^{18}O$ value similar to the rim
361 domains (Figs. 4d and 6), and coexisting secondary mineral phases are absent (Figs.
362 2c-f and 3).

363 (4) Magma mixing can produce textural and compositional zoning in apatite
364 (Tepper and Kuehner 1999; Słaby et al. 2012; Bruand et al. 2014; Laurent et al. 2017),
365 accounting for sharp compositional variations like those observed in apatite from the
366 Zhangzhou granite. Experimental results have shown nonlinear element exchange
367 between the interacting magmas due to variations in diffusion behavior (De Campos

et al. 2008; Perugini et al. 2008). The direction of compositional change in mineral compositions is largely a reflection of the new bulk magma composition after each mixing step and might reverse trends expected from fractional crystallization (with or without crustal contamination) alone. In the case of the Zhangzhou granite, magma mixing is strongly supported by the presence of MMEs and granodiorite inclusions in the monzogranite, at the locality from which the samples were taken (Fig. 2a and b). Mixing is also reflected in abrupt ΣREE variations in the zoned titanite (Supplementary Materials). Thus, magma mixing is our preferred model in explaining the composition zonations that we see in apatite from the Zhangzhou granite.

Composition of end-member melts during magma mixing

The rapid core to rim increases in SiO_2, REE and Y concentrations and decreases in SO_3 and Li of apatite from the Zhangzhou granite can probably be attributed to abrupt changes in bulk melt composition and/or the resultant change in partition coefficients during the apatite crystallization (Fig. 5). For simplicity, we assume a single mixing event and name the magma that crystallized the apatite cores as Batch I, and the mixed magma that crystallized the apatite rims as Batch II.

Previous studies have demonstrated that the REE contents in apatite are primarily controlled by magma composition and mineral/melt partition coefficients (D) (Sha and Chappell 1999; Prowatke and Klemme 2006). Increasing SiO_2 content in a fractionating melt is expected to promote the coupled substitution reaction: $REE^{3+}+SiO_4^{4-} = Ca^{2+} + PO_4^{3-}$ (Pan and Fleet 2002), and to further increase the degree

389 to which REE preferentially partition into apatite rather than melt (i.e., increasing D
390 $^{\mathrm{Ap/melt}}_{\mathrm{REE}}$) (Prowatke and Klemme 2006). Experimental results have also shown that $D_{\mathrm{REE}}^{\mathrm{Ap/melt}}$
391 values depend largely on the composition of magma, showing a strong positive
392 correlation with silica content of magma (e.g., Watson and Green 1981; Prowatke and
393 Klemme 2006; Laurent et al. 2017). This is consistent with the previous investigations
394 on apatite from a wide range of magmatic suites, which found that REE
395 concentrations in apatite increase from the primitive to evolved rocks (Sha and
396 Chappell 1999; Belousova et al. 2002; Chu et al. 2009; Zhang et al. 2020). Therefore,
397 apatite crystallized from a high-SiO_2 magma tends to contain high SiO_2 and REE
398 concentrations (Ladenburger et al. 2016). Given that the ∑REE and SiO_2
399 concentration of apatite rims can be three times higher than cores (Fig. 5b, f and g),
400 we suggest that the SiO_2 content of Batch II magma was relatively high, with a
401 correspondingly high $D_{\mathrm{REE}}^{\mathrm{Ap/melt}}$.

402 Theoretically, sulfur concentration in apatite depends largely on the S content of
403 the melt and it can be used as a proxy to track the sulfur evolution of magma (Parat et
404 al. 2002, 2011; Van Hoose et al. 2013; Brounce et al. 2019). The partition coefficient
405 of sulfur in apatite ($D_{\mathrm{S}}^{\mathrm{Ap/melt}}$) is additionally controlled by complex physio-chemical
406 conditions, including oxygen fugacity (fO_2) and temperature (Peng et al. 1997; Parat
407 and Holtz 2004). Both apatite core and rim domains show similar Eu/Eu* and Ce/Ce*
408 (Fig. 4d), probably suggesting crystallization under similar oxidizing conditions (e.g.,
409 Sha and Chappell 1999; Cao et al. 2012). On the other hand, because the apatite cores
410 and rims occur in the same samples, the similar apatite saturation temperature should

411 have little effect on $D_S^{Ap/melt}$. Therefore, the high S content in apatite cores, which can
412 be four times higher than the apatite rims, is likely attributed to higher sulfur
413 concentration in Batch I magma (Figs. 5c and 7).

414 **Constraints on the magma source**

415 Both core and rim domains in apatite from the Zhangzhou granite exhibit
416 mantle-like $\delta^{18}O$ values in equilibrium with the coeval zircon (Fig. 6, Supplementary
417 Table S3). The granites have whole-rock $^{87}Sr/^{86}Sr_{(i)}$ and $\varepsilon_{Nd}(t)$ values similar to those
418 of MMEs and mafic rocks in the Zhangzhou batholith (Chen et al. 2013). These
419 geochemical features suggest derivation of the Zhangzhou granite from newly
420 accreted crust.

421 As mentioned early, the core and rim domains in apatite from the Zhangzhou
422 granite have distinct chemical compositions, especially the high SO_3 content (up to
423 1.00%) in the core domain. Apatite incorporates sulfur in multiple oxidation states
424 (i.e., S^{6+}, S^{4-} and S^{2-}) via complex substitutions (Piccoli and Candela 2002; Konecke
425 et al. 2017; Brounce et al. 2019). However, previous studies have shown that apatite
426 favors coupled substitution mechanisms involving oxidized S (Streck and Dilles 1998;
427 Kim et al. 2017) and S-rich apatite always crystallizes at a high oxygen fugacity (e.g.,
428 Parat et al. 2011; Chelle-Michou and Chiaradia 2017). This is consistent with the
429 oxidized nature of the I-type, or magnetite-series, Zhangzhou granite (e.g., Ishlhara
430 1977; Carmichael 1991; Blevin and Chappell 1995).

431 At subduction zones, seawater sulfate can be absorbed by the sediments

overlying the mafic oceanic crust during seafloor hydrothermal alteration. During subduction of the oceanic crust and overlying sulfate-bearing sediments, oxidized sulfur is released into the mantle wedge (e.g., Sasaki and Ishihara 1979; de Hoog et al. 2001; Wallace and Edmonds 2011). Arc mafic magmas derived from the mantle wedge metasomatized by sulfate-bearing sediments should correspondingly contain high S (e.g., Sharma et al. 2004), consistent with previous experiments that oxidized arc mafic magmas have a high capacity to contain sulfur (Jugo et al. 2005). For instance, olivine-hosted melt inclusions from the arc mafic magmas can contain high S content up to 7000 ppm (Wallace and Edmonds 2011). An oxidized mafic melt can transport large amounts of sulfur from the mantle to shallow crustal levels and even to the atmosphere (e.g., de Hoog et al. 2004; Richards 2015; Zellmer et al. 2015). Underplated mafic magmas might be the source of high-S arc crust formed during the subduction of paleo-Pacific Ocean in the Cretaceous. Previous studies have also suggested that mafic intrusions might supply sulfur to long-lived felsic magma chambers (Edmonds et al. 2010; Wallace and Edmonds 2011), in which high-S apatite crystallizes (Van Hoose et al. 2013). Thus, underplated mafic magmas releasing S-rich fluid and/or resultant melting of the high-S arc crust could have been the source of the high-S felsic Batch I magma that crystallizes the cores of apatite in the Zhangzhou granite.

Devolatilization of Batch II magma

Liquid-vapour fractionation is considered to be an important process of

453 magmatic differentiation where a separate vapor phase coexists with a magma
454 (Webster and Vivo 2002; Baker and Alletti 2012). This process can cause geochemical
455 variations related to difference in element partitioning between the coexisting vapor
456 and magma. In the case of the Zhangzhou granite, liquid-vapour fractionation
457 probably contributes to the large variations in concentrations of fluid-mobile elements
458 such as S, Cl and Li in the apatite.

459 As discussed above, Batch II magma had higher SiO_2 but lower S than Batch I
460 magma. Considering the evidence, based on tightly constrained isotopic variations,
461 that both magma batches shared a common source, there must have been an additional
462 geological process that rapidly decreases the S content during the evolution of Batch
463 II magma. Possible mechanisms to reduce the S content of magma include: (1)
464 fractionation of sulfide and sulfate (e.g., anhydrite and pyrite); and (2) devolatilization
465 (evaporation of magmatic H_2S and/or SO_2-rich fluid exsolution). Since anhydrite and
466 pyrite are not observed in the studied samples, it seems unlikely that the granitic
467 magma was saturated in sulfide or sulfate minerals. Hence, the reduced S content is
468 unlikely to be supplied by sulfate and sulfide fractionation. Therefore, SO_2
469 disproportionation in an exsolved fluid (e.g., Mavrogenes and Blundy 2017) and/or
470 direct degassing as magmatic H_2S (e.g., Oppenheimer et al. 2011), might be realistic
471 alternative means of lowering the S content in Batch II magma. The oxidation state of
472 I-type granitic magma implies that the majority of S in the magma existed as SO_4^{2-}
473 instead of H_2S (Baker and Moretti 2011; Richards 2015), suggesting a more important
474 role of fluid exsolution than degassing of H_2S during magmatic evolution.

475 Since Cl preferentially partitions into fluids but F is soluble in melts (Baker and
476 Alletti 2012; Webster et al. 2018), devolatilization can also lead to a decrease in Cl
477 concentration of a melt, and in any crystallizing apatite, without significantly
478 affecting F concentrations (e.g., Piccoli and Candela 2002; Webster 2004; Aiuppa et
479 al. 2009; Balcone-Boissard et al. 2010; Zhang et al. 2012; Teiber et al. 2014; Wang et
480 al. 2018). Apatite rims have lower Cl content and Cl/F than the core for any given
481 zoned apatite, consistent with the effect of devolatilization (Fig. 5d and
482 Supplementary Table S2). The indistinguishable ranges in F and Cl concentrations of
483 all apatites (Fig. 4a) are probably due to variable crystallization conditions (Boyce et
484 al. 2014).

485 Devolatilization is also evidenced by the lower Li concentration in the apatite
486 rims (Fig. 5i). Since Li preferentially enters aqueous fluid rather than the silicate melt,
487 devolatilization would lead to a Li decrease in both the melt and crystallizing apatite
488 (Webster et al. 1989; Duan and Jiang 2018). Collectively, Barch II magma
489 experienced strong devolatilization, which is consistent with the previous
490 observations that exsolved fluids have the capacity to sequester Li, Cl and S away
491 from the magmatic systems (e.g., Bai and Koster van Groos 1999; Kamenetsky et al.
492 1999; Webster 2004; Zajacz et al. 2008; Pokrovski et al. 2013).

493 **Petrogenetic implications**

494 It is commonly assumed that elevated $\varepsilon_{Nd}(t)$ or $\varepsilon_{Hf}(t)$ values in granitoids implies
495 mixing by mantle-derived magma, whereas more constant isotopic compositions in

granite reflects the predominant role of fractional crystallization. For example, various degrees of mixing between mantle-derived mafic and crust-derived felsic magmas result in a wide $\varepsilon_{Hf}(t)$ range of the calc-alkaline felsic rocks in SE China (Griffin et al. 2002; Guo et al. 2012). However, in many magmatic systems and tectonic environments, interaction of cogenetic magmas is also inevitable as magma chambers are incrementally, or episodically, filled by magma batches from common sources over time (Taylor 2004; Annen 2009; Farina et al. 2012). In such cases, important magmatic processes such as crystal-melt segregation, liquid-vapor fractionation and self-mixing in crustal magma chamber can be difficult to monitor by traditional bulk-rock geochemical analyses (Turner and Campbell 1986; Couch et al. 2001; Alves et al. 2009; Edmonds and Woods 2018; Sun et al. 2019; Yan et al. 2020). Mixing of cogenetic granitic magmas and devolatilization process, as shown here for the Zhangzhou granite, have occurred with little or no isotopic variation.

More recent studies on granite petrogenesis have benefited from advances in analytical techniques that enable *in-situ* analysis of minerals for stable and radiogenic isotopes, including O, S, Rb-Sr, Sm-Nd and Lu-Hf systems (e.g., Griffin et al. 2002; Yang et al. 2014; Economos et al. 2017; Bruand et al. 2019; Cao et al. 2019). Such studies have shown that *in-situ* geochemical analysis on minerals (e.g., apatite, plagioclase, zircon and titanite) has many advantages over whole-rock chemistry in petrogenetic discussion (e.g., Yu et al. 2018; Gros et al. 2020; Zhang et al. 2020). Apatite performs particularly well as a recorder of petrogenetic processes and our study provides an example illustrating the advantages of using compositional

518 zonations in apatite to track obscure magma processes such as mixing of cogenetic
519 granitic magmas and devolatilization. There is no doubt that *in-situ* compositional and
520 isotopic analysis of apatite will provide significant advances in the range of data
521 available for understanding igneous petrogenesis.
522

523 **FUNDING**

524 This study was financially supported by the National Natural Science Foundation
525 of China (Grant No. 41525006, 42073032 and U1701641) and the Strategic Priority
526 Research Program (B) of Chinese Academy of Sciences (Grant XDB 18000000) to
527 Feng Guo.

528 **ACKNOWLEDGMENTS**

529 We thank Linli Chen and Pengli He for EMPA, Dan Wu for LA-ICPMS, Le
530 Zhang for LA-MC-ICPMS, Jiao Li, Qiuli Li, Zexian Cui and Xiaoping Xia for SIMS
531 analysis. Dr. Xuan-Ce Wang is thanked for discussion. We kindly appreciate the
532 constructive reviews and comments from Prof. Ewa Slaby and an anonymous referee,
533 and manuscript handling by Drs. Don R. Baker and Justin Filiberto. Thanks are also
534 due to Dr. Hugh Smithies who help clarify the expression and polish the language.
535

References cited

Aiuppa, A., Baker, D.R., and Webster, J.D. (2009) Halogens in volcanic systems. Chemical Geology, 263, 1–18.

Alves, A., de Assis Janasi, V., Simonetti, A., and Heaman, L. (2009) Microgranitic enclaves as products of self-mixing events: a study of open-system processes in the Maua granite, Sao Paulo, Brazil, based on in situ isotopic and trace elements in plagioclase. Journal of Petrology, 50, 2221–2247.

Annen, C. (2009) From plutons to magma chambers: Thermal constraints on the accumulation of eruptible silicic magma in the upper crust. Earth and Planetary Science Letters, 284, 409–416.

Ansberque, C., Mark, C., Caulfield, J.T., and Chew, D.M. (2019) Combined in-situ determination of halogen (F, Cl) content in igneous and detrital apatite by SEM-EDS and LA-Q-ICPMS: A potential new provenance tool. Chemical Geology.

Ayers, J.C., and Watson, E.B. (1993) Apatite/fluid partitioning of rare-earth elements and strontium: Experimental results at 1.0 GPa and 1000°C and application to models of fluid-rock interaction. Chemical Geology, 110, 299–314.

Bai, T.B., and Koster van Groos, A.F. (1999) The distribution of Na, K, Rb, Sr, Al, Ge, Cu, W, Mo, La, and Ce between granitic melts and coexisting aqueous fluids.

555 Geochimica et Cosmochimica Acta, 63, 1117–1131.

556 Baker, D.R., and Alletti, M. (2012) Fluid saturation and volatile partitioning between
557 melts and hydrous fluids in crustal magmatic systems: The contribution of
558 experimental measurements and solubility models. Earth-Science Reviews, 114,
559 298–324.

560 Baker, D.R., and Moretti, R. (2011) Modeling the solubility of sulfur in magmas: A
561 50-year old geochemical challenge. Reviews in Mineralogy and Geochemistry,
562 73, 167–213.

563 Balcone-Boissard, H., Villemant, B., and Boudon, G. (2010) Behavior of halogens
564 during the degassing of felsic magmas. Geochemistry, Geophysics, Geosystems,
565 11.

566 Belousova, E.A., Griffin, W.L., O'Reilly, S.Y., and Fisher, N.I. (2002) Apatite as an
567 indicator mineral for mineral exploration: trace-element compositions and their
568 relationship to host rock type. Journal of Geochemical Exploration, 76, 45–69.

569 Birski, Ł., Słaby, E., Wirth, R., Koch-Müller, M., Simon, K., Wudarska, A., Götze, J.,
570 Lepland, A., Hofmann, A., and Kuras, A. (2019) Archaean phosphates: a case
571 study of transformation processes in apatite from the Barberton greenstone belt.
572 Contributions to Mineralogy and Petrology, 174, 25.

573 Blevin, P.L., and Chappell, B.W. (1995) Chemistry, origin, and evolution of
574 mineralized granites in the Lachlan fold belt, Australia; the metallogeny of I- and

S-type granites. Economic Geology, 90, 1604–1619.

Boyce, J.W., Tomlinson, S.M., McCubbin, F.M., Greenwood, J.P., and Treiman, A.H. (2014) The Lunar Apatite Paradox. Science, 344, 400–402.

Broom-Fendley, S., Heaton, T., Wall, F., and Gunn, G. (2016) Tracing the fluid source of heavy REE mineralisation in carbonatites using a novel method of oxygen-isotope analysis in apatite: The example of Songwe Hill, Malawi. Chemical Geology, 440, 275–287.

Brounce, M., Boyce, J., McCubbin, F.M., Humphreys, J., Reppart, J., Stolper, E., and Eiler, J. (2019) The oxidation state of sulfur in lunar apatite. American Mineralogist, 104, 307–312.

Bruand, E., Storey, C., and Fowler, M. (2014) Accessory mineral chemistry of high Ba-Sr granites from northern Scotland: Constraints on petrogenesis and records of whole-rock signature. Journal of Petrology, 55, 1619–1651.

Bruand, E., Fowler, M., Storey, C., and Darling, J. (2017) Apatite trace element and isotope applications to petrogenesis and provenance. American Mineralogist, 102, 75–84.

Bruand, E., Storey, C., Fowler, M., and Heilimo, E. (2019) Oxygen isotopes in titanite and apatite, and their potential for crustal evolution research. Geochimica et Cosmochimica Acta, 255, 144–162.

Cao, M., Li, G., Qin, K., Seitmuratova, E.Y., and Liu, Y. (2012) Major and trace

element characteristics of apatites in granitoids from central Kazakhstan: Implications for petrogenesis and mineralization. Resource Geology, 62, 63–83.

Cao, M., Evans, N.J., Qin, K., Danišík, M., Li, G., and McInnes, B.I.A. (2019) Open apatite Sr isotopic system in low-temperature hydrous regimes. Journal of Geophysical Research: Solid Earth, 124, 11192–11203.

Carmichael, I.S.E. (1991) The redox states of basic and silicic magmas: a reflection of their source regions? Contributions to Mineralogy and Petrology, 106, 129–141.

Chappell, B.W., and White, A.J.R. (1974) Two contrasting granite types. Pacific geology, 8(2), 173-174.

Chelle-Michou, C., and Chiaradia, M. (2017) Amphibole and apatite insights into the evolution and mass balance of Cl and S in magmas associated with porphyry copper deposits. Contributions to Mineralogy and Petrology, 172.

Chen, J.-Y., Yang, J.-H., Zhang, J.-H., Sun, J.-F., and Wilde, S.A. (2013) Petrogenesis of the Cretaceous Zhangzhou batholith in southeastern China: Zircon U–Pb age and Sr–Nd–Hf–O isotopic evidence. Lithos, 162–163, 140–156.

Cherniak, D.J. (2010) Diffusion in accessory minerals: Zircon, titanite, apatite, monazite and xenotime. Reviews in Mineralogy and Geochemistry, 72, 827–869.

Chu, M.F., Wang, K.L., Griffin, W.L., Chung, S.L., O'Reilly, S.Y., Pearson, N.J., and Iizuka, Y. (2009) Apatite composition: Tracing petrogenetic processes in Transhimalayan granitoids. Journal of Petrology, 50, 1829–1855.

615 Couch, S., Sparks, R.S.J., and Carroll, M.R. (2001) Mineral disequilibrium in lavas
616 explained by convective self-mixing in open magma chambers. Nature, 411,
617 1037–1039.

618 De Campos, C.P., Dingwell, D.B., Perugini, D., Civetta, L., and Fehr, T.K. (2008)
619 Heterogeneities in magma chambers: Insights from the behavior of major and
620 minor elements during mixing experiments with natural alkaline melts. Chemical
621 Geology, 256, 131–145.

622 De Hoog, J.C.M., Mason, P.R.D., and van Bergen, M.J. (2001) Sulfur and chalcophile
623 elements in subduction zones: constraints from a laser ablation ICP-MS study of
624 melt inclusions from Galunggung Volcano, Indonesia. Geochimica et
625 Cosmochimica Acta, 65, 3147–3164.

626 De Hoog, J.C.M., Hattori, K.H., and Hoblitt, R.P. (2004) Oxidized sulfur-rich mafic
627 magma at Mount Pinatubo, Philippines. Contributions to Mineralogy and
628 Petrology, 146, 750–761.

629 DePaolo, D.J. (1981) Trace element and isotopic effects of combined wallrock
630 assimilation and fractional crystallization. Earth and Planetary Science Letters,
631 53, 189–202.

632 Dowty, E. (1980) Crystal-chemical factors affecting the mobility of ions in minerals.
633 American Mineralogist, 65, 174–182.

634 Duan, D.-F., and Jiang, S.-Y. (2018) Using apatite to discriminate synchronous

ore-associated and barren granitoid rocks: A case study from the Edong metallogenic district, South China. Lithos, 310–311, 369–380.

Economos, R., Boehnke, P., and Burgisser, A. (2017) Sulfur isotopic zoning in apatite crystals: A new record of dynamic sulfur behavior in magmas. Geochimica et Cosmochimica Acta, 215, 387–403.

Edmonds, M., and Woods, A.W. (2018) Exsolved volatiles in magma reservoirs. Journal of Volcanology and Geothermal Research, 368, 13–30.

Edmonds, M., Aiuppa, A., Humphreys, M., Moretti, R., Giudice, G., Martin, R.S., Herd, R.A., and Christopher, T. (2010) Excess volatiles supplied by mingling of mafic magma at an andesite arc volcano. Geochemistry, Geophysics, Geosystems, 11.

Elburg, M., Vroon, P., van der Wagt, B., and Tchalikian, A. (2005) Sr and Pb isotopic composition of five USGS glasses (BHVO-2G, BIR-1G, BCR-2G, TB-1G, NKT-1G). Chemical Geology, 223, 196–207.

Farina, F., Stevens, G., and Villaros, A. (2012) Multi-batch, incremental assembly of a dynamic magma chamber: the case of the Peninsula pluton granite (Cape Granite Suite, South Africa). Mineralogy and Petrology, 106, 193–216.

Ferry, J.M., and Watson, E.B. (2007) New thermodynamic models and revised calibrations for the Ti-in-zircon and Zr-in-rutile thermometers. Contributions to Mineralogy and Petrology, 154, 429–437.

Gao, Y., Hoefs, J., Hellebrand, E., von der Handt, A., and Snow, J.E. (2007) Trace

element zoning in pyroxenes from ODP Hole 735B gabbros: diffusive exchange or synkinematic crystal fractionation? Contributions to Mineralogy and Petrology, 153, 429–442.

Griffin, W.L., Wang, X., Jackson, S.E., Pearson, N.J., O'Reilly, S.Y., Xu, X., and Zhou, X. (2002) Zircon chemistry and magma mixing, SE China: In-situ analysis of Hf isotopes, Tonglu and Pingtan igneous complexes. Lithos, 61, 237–269.

Gros, K., Słaby, E., Birski, Ł., Kozub-Budzyń, G., and Sláma, J. (2020) Geochemical evolution of a composite pluton: insight from major and trace element chemistry of titanite. Mineralogy and Petrology, 114(5): 375-401.

Guo, F., Nakamuru, E., Fan, W., Kobayoshi, K., and Li, C. (2007) Generation of palaeocene adakitic andesites by magma mixing; Yanji Area, NE China. Journal of Petrology, 48, 661–692.

Guo, F., Fan, W., Li, C., Zhao, L., Li, H., and Yang, J. (2012) Multi-stage crust–mantle interaction in SE China: Temporal, thermal and compositional constraints from the Mesozoic felsic volcanic rocks in eastern Guangdong–Fujian provinces. Lithos, 150, 62–84.

Harlov, D.E. (2015) Apatite: A fingerprint for metasomatic processes. Elements, 11, 171–176.

Harlov, D.E., and Förster, H.-J. (2003) Fluid-induced nucleation of (Y+REE)-phosphate minerals within apatite: Nature and experiment. Part II.

676 Fluorapatite. American Mineralogist, 88, 1209–1229.

677 Harlov, D.E., Wirth, R., and Förster, H.-J. (2005) An experimental study of
678 dissolution–reprecipitation in fluorapatite: fluid infiltration and the formation of
679 monazite. Contributions to Mineralogy and Petrology, 150, 268–286.

680 Ishlhara, S. (1977) The Magnetite-series and Ilmenite-series Granitic Rocks. Mining
681 Geology, 27, 293–305.

682 Jugo, P.J., Luth, R.W., and Richards, J.P. (2005) An experimental study of the sulfur
683 content in basaltic melts saturated with immiscible sulfide or sulfate liquids at
684 1300°C and 10 GPa. Journal of Petrology, 46, 783–798.

685 Jung, S., Hoernes, S., Masberg, P., and Hoffer, E. (1999) The petrogenesis of some
686 migmatites and granites (Central Damara Orogen, Namibia): Evidence for
687 disequilibrium melting, wall-rock contamination and crystal fractionation.
688 Journal of Petrology, 40, 1241–1269.

689 Kamenetsky, V.S., Wolfe, R.C., Eggins, S.M., Mernagh, T.P., and Bastrakov, E. (1999)
690 Volatile exsolution at the Dinkidi Cu-Au porphyry deposit, Philippines: A
691 melt-inclusion record of the initial ore-forming process. Geology, 27, 691–694.

692 Kim, Y., Konecke, B., Fiege, A., Simon, A., and Becker, U. (2017) An ab-initio study
693 of the energetics and geometry of sulfide, sulfite, and sulfate incorporation into
694 apatite: The thermodynamic basis for using this system as an oxybarometer.
695 American Mineralogist, 102, 1646–1656.

696 Konecke, B.A., Fiege, A., Simon, A.C., Parat, F., and Stechern, A. (2017)
697 Co-variability of S^{6+}, S^{4+}, and S^{2-} in apatite as a function of oxidation state:
698 Implications for a new oxybarometer. American Mineralogist, 102, 548–557.
699 Ladenburger, S., Marks, M.A.W., Upton, B., Hill, P., Wenzel, T., and Markl, G. (2016)
700 Compositional variation of apatite from rift-related alkaline igneous rocks of the
701 Gardar Province, South Greenland. American Mineralogist, 101, 612–626.

702 Laurent, O., Zeh, A., Gerdes, A., Villaros, A., Gros, K., and Slaby, E. (2017) How do
703 granitoid magmas mix with each other? Insights from textures, trace element and
704 Sr–Nd isotopic composition of apatite and titanite from the Matok pluton (South
705 Africa). Contributions to Mineralogy and Petrology, 172, 80.

706 Li, X.-H., Li, Z.-X., Wingate, M.T.D., Chung, S.-L., Liu, Y., Lin, G.-C., and Li, W.-X.
707 (2006) Geochemistry of the 755Ma Mundine Well dyke swarm, northwestern
708 Australia: Part of a Neoproterozoic mantle superplume beneath Rodinia?
709 Precambrian Research, 146, 1–15.

710 Li, X.-H., Li, W.-X., Li, Q.-L., Wang, X.-C., Liu, Y., and Yang, Y.-H. (2010)
711 Petrogenesis and tectonic significance of the ~850 Ma Gangbian alkaline
712 complex in South China: Evidence from in situ zircon U–Pb dating, Hf–O
713 isotopes and whole-rock geochemistry. Lithos, 114, 1–15.

714 Li, Z., Qiu, J.S., and Yang, X.M. (2014) A review of the geochronology and
715 geochemistry of Late Yanshanian (Cretaceous) plutons along the Fujian coastal

area of southeastern China: Implications for magma evolution related to slab break-off and rollback in the Cretaceous. Earth-Science Reviews, 128, 232–248.

Lisowiec, K., Slaby, E., and Förster, H.J. (2015) Polytopic Vector Analysis (PVA) modelling of whole-rock and apatite chemistry from the Karkonosze composite pluton (Poland, Czech Republic). Lithos, 230, 105–120.

Liu, Y. (1996) Simultaneous and precise determination of 40 trace elements in rock samples using ICP-MS. Geochimica, 25, 552–558 (In Chinese with English abstract).

Liu, Y.S., Hu, Z.C., Gao, S., Gunther, D., Xu, J., Gao, C.G., and Chen, H.H. (2008) In situ analysis of major and trace elements of anhydrous minerals by LA-ICP-MS without applying an internal standard. Chemical Geology, 257, 34–43.

Marks, M.A.W., Wenzel, T., Whitehouse, M.J., Loose, M., Zack, T., Barth, M., Worgard, L., Krasz, V., Eby, G.N., Stosnach, H., and others (2012) The volatile inventory (F, Cl, Br, S, C) of magmatic apatite: An integrated analytical approach. Chemical Geology, 291, 241–255.

Mavrogenes, J., and Blundy, J. (2017) Crustal sequestration of magmatic sulfur dioxide. Geology, 45, 211–214.

Nash, W.P., and Crecraft, H.R. (1985) Partition coefficients for trace elements in silicic magmas. Geochimica et Cosmochimica Acta, 49, 2309–2322.

Nathwani, C.L., Loader, M.A., Wilkinson, J.J., Buret, Y., Sievwright, R.H., and

736 Hollings, P. (2020) Multi-stage arc magma evolution recorded by apatite in
737 volcanic rocks. Geology, 48, 323–327.

738 Oppenheimer, C., Scaillet, B., and Martin, R.S. (2011) Sulfur degassing from
739 volcanoes: Source conditions, surveillance, plume chemistry and Earth system
740 impacts. Reviews in Mineralogy and Geochemistry, 73, 363–421.

741 Pan, Y., and Fleet, M.E. (2002) Compositions of the apatite-group minerals:
742 Substitution mechanisms and controlling factors. Reviews in Mineralogy and
743 Geochemistry, 48, 13–49.

744 Parat, F., and Holtz, F. (2004) Sulfur partitioning between apatite and melt and effect
745 of sulfur on apatite solubility at oxidizing conditions. Contributions to
746 Mineralogy and Petrology, 147, 201–212.

747 Parat, F., Dungan, M.A., and Streck, M.J. (2002) Anhydrite, pyrrhotite, and sulfur-rich
748 apatite: tracing the sulfur evolution of an Oligocene andesite (Eagle Mountain,
749 CO, USA). Lithos, 64, 63–75.

750 Parat, F., Holtz, F., and Streck, M.J. (2011) Sulfur-bearing magmatic accessory
751 minerals. Reviews in Mineralogy and Geochemistry, 73, 285–314.

752 Peng, G., Luhr, J.F., and McGee, J.J. (1997) Factors controlling sulfur concentrations
753 in volcanic apatite. American Mineralogist, 82, 1210–1224.

754 Perugini, D., De Campos, C.P., Dingwell, D.B., Petrelli, M., and Poli, G. (2008) Trace
755 element mobility during magma mixing: Preliminary experimental results.

Chemical Geology, 256, 146–157.

Piccoli, P.M., and Candela, P.A. (2002) Apatite in igneous systems. Reviews in Mineralogy and Geochemistry, 48, 255–292.

Pokrovski, G.S., Borisova, A.Y., and Bychkov, A.Y. (2013) Speciation and transport of metals and metalloids in geological vapors. Reviews in Mineralogy and Geochemistry, 76, 165–218.

Prowatke, S., and Klemme, S. (2006) Trace element partitioning between apatite and silicate melts. Geochimica et Cosmochimica Acta, 70, 4513–4527.

Rae, D.A., Coulson, I.M., and Chambers, A.D. (1996) Metasomatism in the North Qôroq centre, South Greenland: apatite chemistry and rare-earth element transport. Mineralogical Magazine, 60, 207–220.

Richards, J.P. (2015) The oxidation state, and sulfur and Cu contents of arc magmas: implications for metallogeny. Lithos, 233, 27–45.

Sasaki, A., and Ishihara, S. (1979) Sulfur isotopic composition of the magnetite-series and ilmenite-series granitoids in Japan. Contributions to Mineralogy and Petrology, 68, 107–115.

Sha, L.-K., and Chappell, B.W. (1999) Apatite chemical composition, determined by electron microprobe and laser-ablation inductively coupled plasma mass spectrometry, as a probe into granite petrogenesis. Geochimica et Cosmochimica Acta, 63, 3861–3881.

776 Sharma, K., Blake, S., Self, S., and Krueger, A.J. (2004) SO_2 emissions from basaltic
777 eruptions, and the excess sulfur issue. Geophysical Research Letters, 31.

778 Słaby, E., Martin, H., Hamada, M., Śmigielski, M., Domonik, A., Götze, J., Hoefs, J.,
779 Hałas, S., Simon, K., Devidal, J.-L., and others (2012) Evidence in Archaean
780 alkali feldspar megacrysts for high-temperature interaction with mantle fluids.
781 Journal of Petrology, 53, 67–98.

782 Streck, M.J. (2008) Mineral textures and zoning as evidence for open system
783 processes. Reviews in Mineralogy and Geochemistry, 69, 595–622.

784 Streck, M.J., and Dilles, J.H. (1998) Sulfur evolution of oxidized arc magmas as
785 recorded in apatite from a porphyry copper batholith. Geology, 26, 523–526.

786 Sun, J.-F., Zhang, J.-H., Yang, J.-H., Yang, Y.-H., and Chen, S. (2019) Tracing magma
787 mixing and crystal–melt segregation in the genesis of syenite with mafic
788 enclaves: Evidence from in situ zircon Hf–O and apatite Sr–Nd isotopes. Lithos,
789 334–335, 42–57.

790 Taylor, R.Z. (2004) Are plutons assembled over millions of years by amalgamation
791 from small magma chambers? Gsa Today, 14, 4.

792 Teiber, H., Marks, M.A.W., Wenzel, T., Siebel, W., Altherr, R., and Markl, G. (2014)
793 The distribution of halogens (F, Cl, Br) in granitoid rocks. Chemical Geology,
794 374–375, 92–109.

795 Tepper, J.H., and Kuehner, S.M. (1999) Complex zoning in apatite from the Idaho

796 Batholith; a record of magma mixing and intracrystalline trace element diffusion.
797 American Mineralogist, 84, 581–595.

798 Trotter, J.A., Williams, I.S., Barnes, C.R., Lécuyer, C., and Nicoll, R.S. (2008) Did
799 cooling oceans trigger ordovician biodiversification? Evidence from conodont
800 thermometry. Science, 321, 550–554.

801 Tu, X.L., Zhang, H., Deng, W.F., Ling, M.X., Liang, H.Y., Liu, Y., and Sun, W.D.
802 (2011) Application of RESOlution in-situ laser ablation ICP-MS in trace element
803 analyses. Geochimica, 40, 83–98 (In Chinese with English abstract).

804 Turner, J.S., and Campbell, I.H. (1986) Convection and mixing in magma chambers.
805 Earth-Science Reviews, 23, 255–352.

806 Van Hoose, A.E., Streck, M.J., Pallister, J.S., and Wälle, M. (2013) Sulfur evolution
807 of the 1991 Pinatubo magmas based on apatite. Journal of Volcanology and
808 Geothermal Research, 257, 72–89.

809 Wallace, P.J., and Edmonds, M. (2011) The sulfur budget in magmas: Evidence from
810 melt inclusions, submarine glasses, and volcanic gas emissions. Reviews in
811 Mineralogy and Geochemistry, 73, 215–246.

812 Wang, L.-X., Ma, C.-Q., Zhang, C., Zhu, Y.-X., and Marks, M.A. (2018) Halogen
813 geochemistry of I-and A-type granites from Jiuhuashan region (South China):
814 Insights into the elevated fluorine in A-type granite. Chemical Geology, 478,

164–182.

Watson, E.B., and Green, T.H. (1981) Apatite/liquid partition coefficients for the rare earth elements and strontium. Earth and Planetary Science Letters, 56, 405–421.

Webster, J.D. (2004) The exsolution of magmatic hydrosaline chloride liquids. Chemical Geology, 210, 33–48.

Webster, J.D., and Piccoli, P.M. (2015) Magmatic apatite: A powerful, yet deceptive, mineral. Elements, 11, 177–182.

Webster, J.D., and Vivo, B.D. (2002) Experimental and modeled solubilities of chlorine in aluminosilicate melts, consequences of magma evolution, and implications for exsolution of hydrous chloride melt at Mt. Somma-Vesuvius. American Mineralogist, 87, 1046–1061.

Webster, J.D., Holloway, J.R., and Hervig, R.L. (1989) Partitioning of lithophile trace elements between H_2O and H_2O+ CO_2 fluids and topaz rhyolite melt. Economic Geology, 84, 116–134.

Webster, J.D., Baker, D.R., and Aiuppa, A. (2018) Halogens in mafic and intermediate-silica content magmas. In D.E. Harlov and L. Aranovich, Eds., The Role of Halogens in Terrestrial and Extraterrestrial Geochemical Processes: Surface, Crust, and Mantle p. 307–430. Springer International Publishing, Cham.

Weis, D., Kieffer, B., Maerschalk, C., Pretorius, W., and Barling, J. (2005) High-precision Pb-Sr-Nd-Hf isotopic characterization of USGS BHVO-1 and

BHVO-2 reference materials. Geochemistry, Geophysics, Geosystems, 6.

Whalen, J.B., Currie, K.L., and Chappell, B.W. (1987) A-type granites: geochemical characteristics, discrimination and petrogenesis. Contributions to Mineralogy and Petrology, 95, 407–419.

Xia, X.-P., Cui, Z.-X., Li, W., Zhang, W.-F., Yang, Q., Hui, H., and Lai, C.-K. (2019) Zircon water content: reference material development and simultaneous measurement of oxygen isotopes by SIMS. Journal of Analytical Atomic Spectrometry, 34, 1088–1097.

Xu, X., Zhao, K., He, Z., Liu, L., and Hong, W. (2020) Cretaceous volcanic-plutonic magmatism in SE China and a genetic model. Lithos, 105728.

Yan, L.-L., He, Z.-Y., Klemd, R., Beier, C., and Xu, X.-S. (2020) Tracking crystal-melt segregation and magma recharge using zircon trace element data. Chemical Geology, 542, 119596.

Yang, Y.-H., Wu, F.-Y., Yang, J.-H., Chew, D.M., Xie, L.-W., Chu, Z.-Y., Zhang, Y.-B., and Huang, C. (2014) Sr and Nd isotopic compositions of apatite reference materials used in U–Th–Pb geochronology. Chemical Geology, 385, 35–55.

Yu, K., Liu, Y., Hu, Q., Ducea, M.N., Hu, Z., Zong, K., and Chen, H. (2018) Magma recharge and reactive bulk assimilation in enclave-bearing granitoids, Tonglu, South China. Journal of Petrology, 59, 795–824.

Zajacz, Z., Halter, W.E., Pettke, T., and Guillong, M. (2008) Determination of fluid/melt partition coefficients by LA-ICPMS analysis of co-existing fluid and

856 silicate melt inclusions: Controls on element partitioning. Geochimica et
857 Cosmochimica Acta, 72, 2169–2197.
858 Zellmer, G.F., Edmonds, M., and Straub, S.M. (2015) Volatiles in subduction zone
859 magmatism. Geological Society, London, Special Publications, 410, 1–17.
860 Zeng, L.-P., Zhao, X.-F., Li, X.-C., Hu, H., and McFarlane, C. (2016) In situ elemental
861 and isotopic analysis of fluorapatite from the Taocun magnetite-apatite deposit,
862 Eastern China: Constraints on fluid metasomatism. American Mineralogist, 101,
863 2468–2483.
864 Zhang, B., Guo, F., Zhang, X., Wu, Y., Wang, G., and Zhao, L. (2019) Early
865 cretaceous subduction of Paleo-Pacific Ocean in the coastal region of SE China:
866 Petrological and geochemical constraints from the mafic intrusions. Lithos, 334,
867 8-24.

868 Zhang, C., Holtz, F., Ma, C.Q., Wolff, P.E., and Li, X.Y. (2012) Tracing the evolution
869 and distribution of F and Cl in plutonic systems from volatile-bearing minerals: a
870 case study from the Liujiawa pluton (Dabie orogen, China). Contributions to
871 Mineralogy and Petrology, 164, 859–879.

872 Zhang, L., Ren, Z.-Y., Xia, X.-P., Li, J., and Zhang, Z.-F. (2015) IsotopeMaker: A
873 Matlab program for isotopic data reduction. International Journal of Mass
874 Spectrometry, 392, 118–124.
875 Zhang, X., Guo, F., Zhang, B., Zhao, L., Wu, Y., Wang, G., and Alemayehu, M. (2020)
876 Magmatic evolution and post-crystallization hydrothermal activity in the early

877 Cretaceous Pingtan intrusive complex, SE China: records from apatite
878 geochemistry. Contributions to Mineralogy and Petrology, 175, 35.

879 Zhang, Yuzhi, Wang, Y., Geng, H., Zhang, Yanhua, Fan, W., and Zhong, H. (2013)
880 Early Neoproterozoic (~850Ma) back-arc basin in the Central Jiangnan Orogen
881 (Eastern South China): Geochronological and petrogenetic constraints from
882 meta-basalts. Precambrian Research, 231, 325–342.

883 Zhou, X.M., Sun, T., Shen, W., Shu, L., and Niu, Y. (2006) Petrogenesis of Mesozoic
884 granitoids and volcanic rocks in south China: a response to tectonic evolution.
885 Episodes, 26–33.

886

List of figure captions

Fig. 1 Simplified geological maps showing tectonic setting (after Zheng et al. 2013), and the distribution of Mesozoic granites in the coastal region of SE China (after Zhou et al., 2006).

Fig. 2 (a-b) Field photos showing the contact relationship between the host granite (monzogranite) and mafic microgranular enclaves. (c-d) Columnar apatite inclusions occurring in biotite and plagioclase. (e-f) BSE images showing zoned apatite hosted in titanite and biotite.

Fig. 3 Representative BSE images of apatite from the Zhangzhou calc-alkaline granite. Most crystals show a core-rim zonation texture.

Fig. 4 Plots of Cl vs. F (a), Cl-OH-F (b), Y vs. Ce (ppm) (c) of apatite, and chondite-normalized REE patterns of apatite (d). In (b) the concentrations of volatile components (atomic proportions) in apatite is estimated by using the method by Piccoli and Candela (2002). In (c), the variation fields of apatite in S-type and I-type granite are from Laurent et al. (2017). Normalization values (d) are from McDonough and Sun (1995).

Fig. 5 Core-to-rim profiles of major and trace element compositions of a zoned apatite crystal from the Zhangzhou calc-alkaline granite. (a) The BSE image showing the core-to-rim analyzed profiles. (b-e) EPMA analysis, variations in SiO_2 (b), SO_3 (c), Cl (d) and Na_2O (e) across the profile. (f-i) LA-ICPMS analysis, variations in Ce (f), Y (g), Sr (h) and Li (i) across the profile.

Fig. 6 Plot of ΣREE (ppm) vs. $\delta^{18}O$, the bars denote the analytical errors given as 2σ.

Fig. 7 Plots of SiO_2 (wt%) vs. SO_3 (wt%).

Supplementary Tables

Table 1 Whole-rock major and trace elements and Sr-Nd isotopic compositions of Zhangzhou Complex, SE China

Table 2 *In-situ* elemental and O isotopic compositions of apatite from Zhangzhou granite

Table 3 *In-situ* elemental and O isotopic compositions of zircon from Zhangzhou granite.

Table 4 *In-situ* major and trace elements compositions of titanite from Zhangzhou granite.

Table 5 *In-situ* elemental and Sr isotopic compositions of plagioclase from

921 Zhangzhou granite.

922

Fig 1

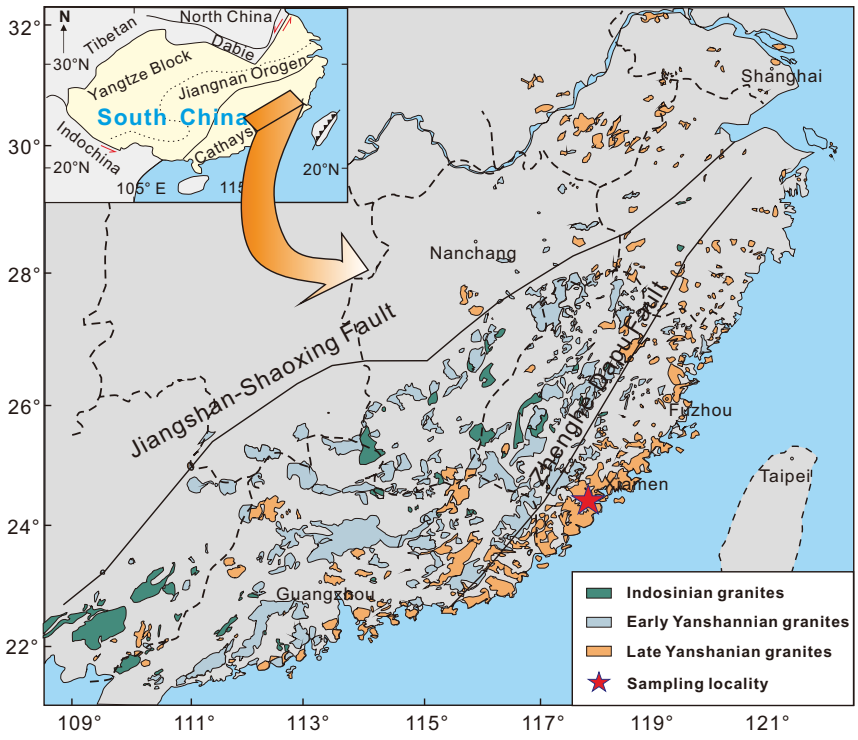

This is the peer-reviewed, final accepted version for American Mineralogist, published by the Mineralogical Society of America.
The published version is subject to change. Cite as Authors (Year) Title. American Mineralogist, in press.
DOI: https://doi.org/10.2138/am-2021-7786. http://www.minsocam.org/

Fig 2

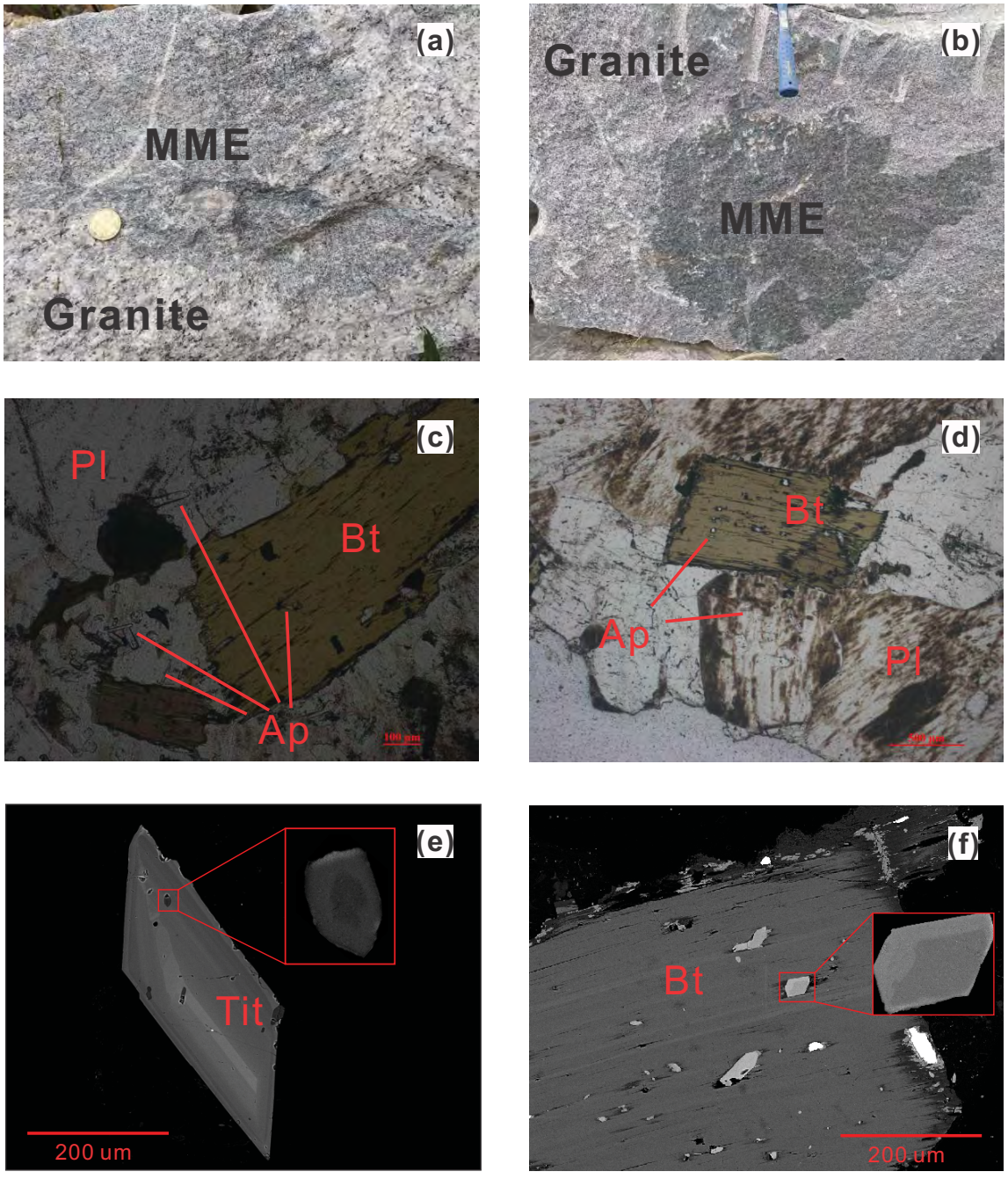

Fig 3

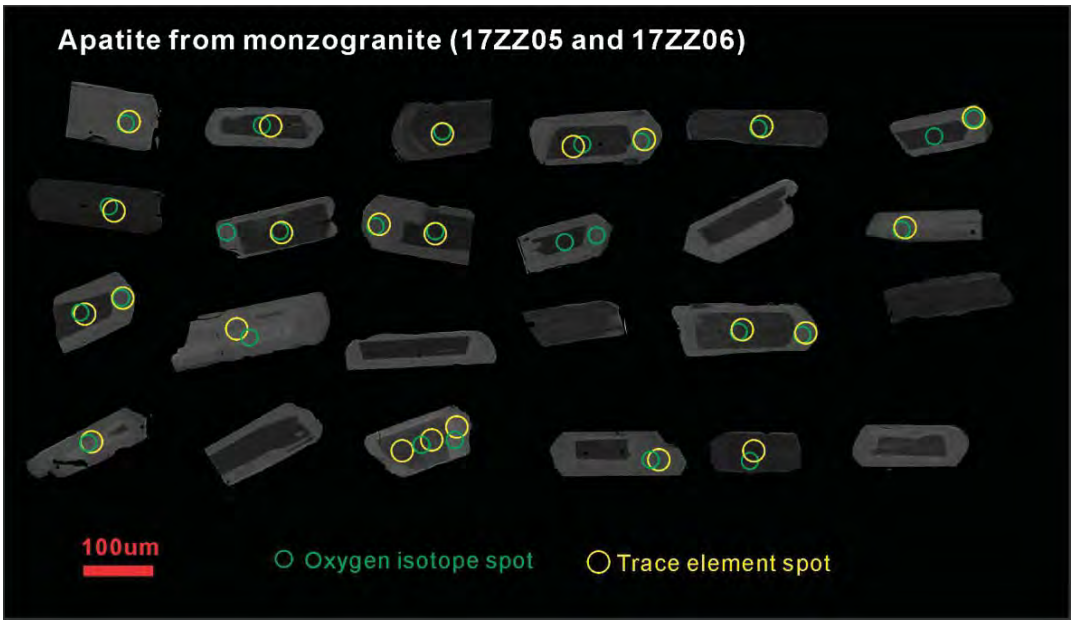

This is the peer-reviewed, final accepted version for American Mineralogist, published by the Mineralogical Society of America.
The published version is subject to change. Cite as Authors (Year) Title. American Mineralogist, in press.
DOI: https://doi.org/10.2138/am-2021-7786. http://www.minsocam.org/

Fig 4

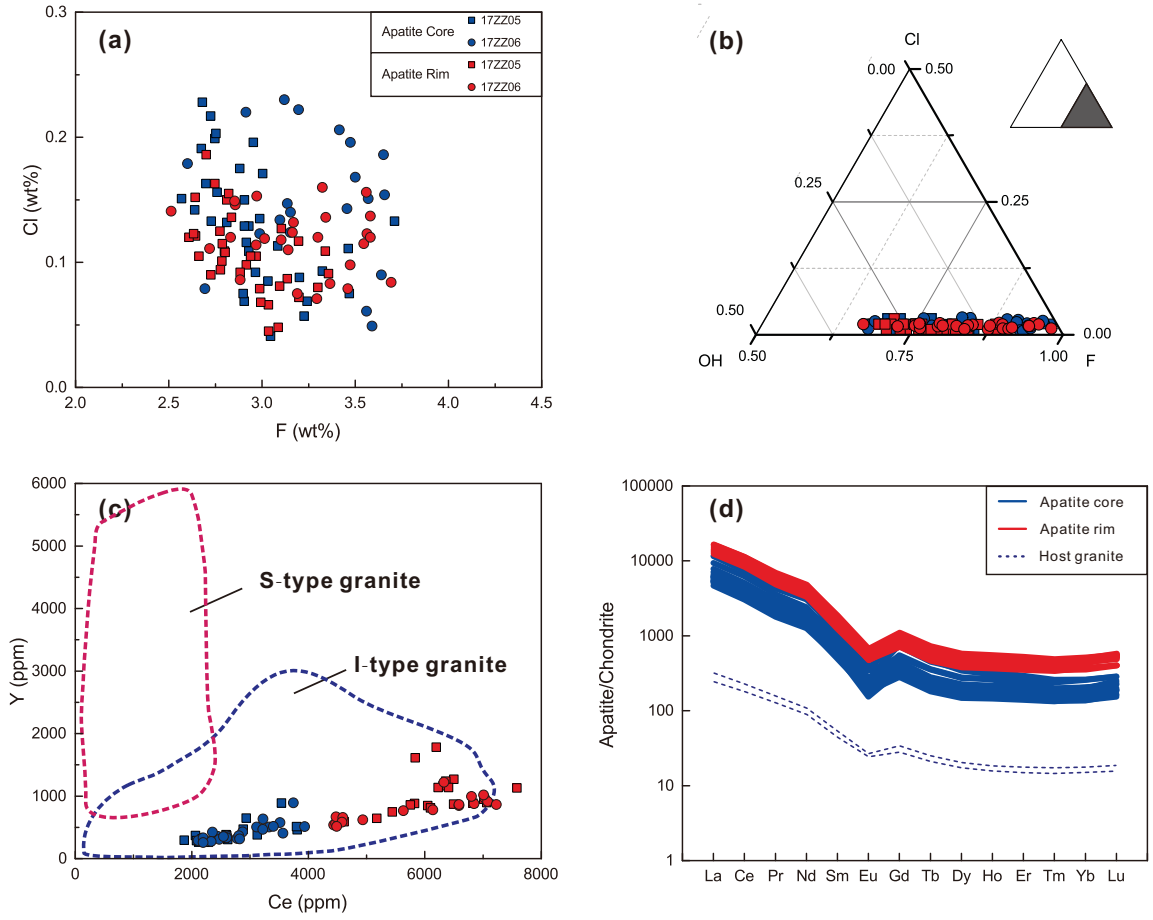

This is the peer-reviewed, final accepted version for American Mineralogist, published by the Mineralogical Society of America.
The published version is subject to change. Cite as Authors (Year) Title. American Mineralogist, in press.
DOI: https://doi.org/10.2138/am-2021-7786. http://www.minsocam.org/

Fig 5

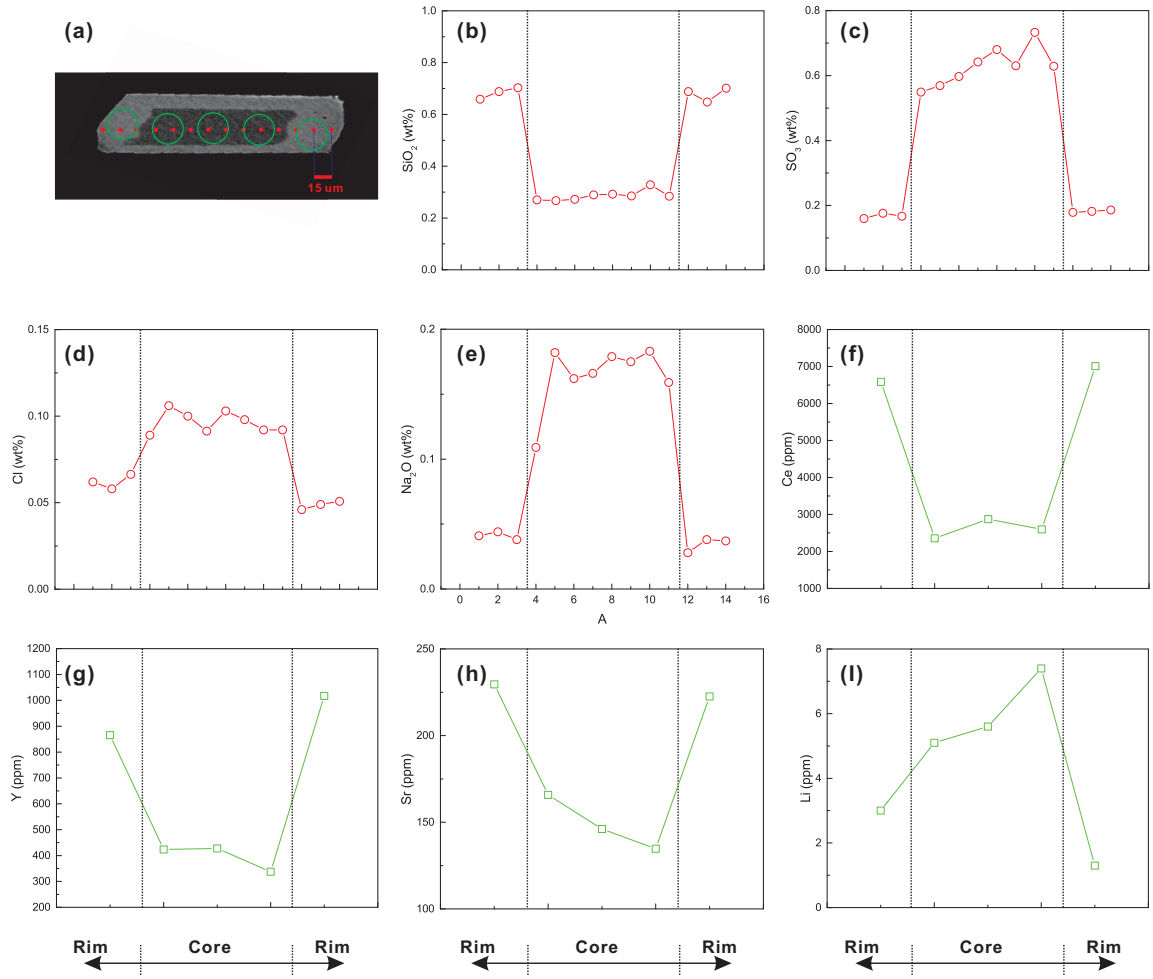

Fig 6

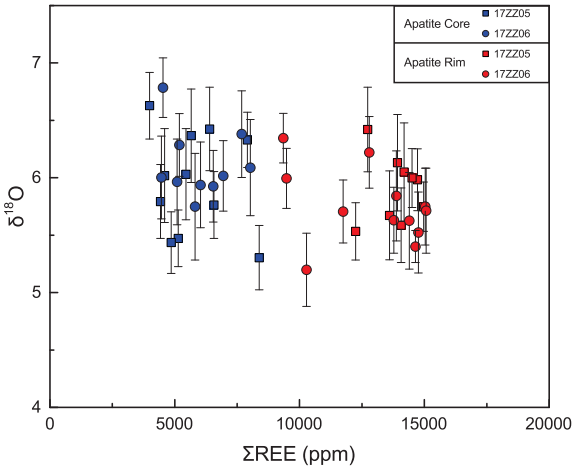

Fig 7